Electron delocalization triggers nonradical Fenton-like catalysis over spinel oxides

Zhi-Yan Guo[a,b,c] (ORCID), Yang Si[a], Wen-Qi Xia[a] (ORCID), Fan Wang[d], Hou-Qi Liu[b], Cheng Yang[a], Wen-Jun Zhang[c], and Wen-Wei Li[a,b,1] (ORCID)

Nonradical Fenton-like catalysis offers opportunities to overcome the low efficiency and secondary pollution limitations of existing advanced oxidation decontamination technologies, but realizing this on transition metal spinel oxide catalysts remains challenging due to insufficient understanding of their catalytic mechanisms. Here, we explore the origins of catalytic selectivity of Fe–Mn spinel oxide and identify electron delocalization of the surface metal active site as the key driver of its nonradical catalysis. Through fine-tuning the crystal geometry to trigger Fe–Mn superexchange interaction at the spinel octahedra, $ZnFeMnO_4$ with high-degree electron delocalization of the Mn–O unit was created to enable near 100% nonradical activation of peroxymonosulfate (PMS) at unprecedented utilization efficiency. The resulting surface-bound PMS* complex can efficiently oxidize electron-rich pollutants with extraordinary degradation activity, selectivity, and good environmental robustness to favor water decontamination applications. Our work provides a molecule-level understanding of the catalytic selectivity and bimetallic interactions of Fe–Mn spinel oxides, which may guide the design of low-cost spinel oxides for more selective and efficient decontamination applications.

spinel oxides | peroxymonosulfate (PMS) | superexchange | delocalization | octahedron

Clean water scarcity is one of the most severe challenges faced by the world today, especially in many underdeveloped countries. Therefore, it is of vital importance to develop efficient and affordable water decontamination technologies, among which advanced oxidation processes (AOPs) aiming at complete destruction of various hazardous pollutants is an indispensable option (1). However, the practical application of conventional AOPs for water treatment, mainly based on the generation of sulfate radicals $(SO_4^{\bullet-})$ and/or hydroxyl radicals $(^{\bullet}OH)$, is severely hindered by poor decontamination selectivity (2, 3). Thus, to ensure sufficient removal of targeted pollutants (e.g., the emerging micropollutants) among various competitive species in real waters, excessive input of oxidant and/or energy is typically adopted, which not only increases the cost but also may result in undesired by-products (4–6). The need to address this challenge has motivated intensive research on selective oxidation technologies via nonradical Fenton-like catalysis, especially peroxymonosulfate (PMS)-based AOPs (7). To date, a number of catalysts for this purpose have been developed but are mainly limited to carbon-based nanomaterials and single-atom catalysts (8–10) which mostly have insufficient stability to suit practical application.

Transition metallic spinel oxides offer a promising alternative, which are earth-abundant, chemically stable, and, most importantly, structurally tunable for various catalytic applications including PMS activation (11–13). However, PMS activation by these materials mostly proceeds via radical pathways, although a few cases of nonradical catalysis have also been reported, and the origins of their discrepant catalytic properties remain unclear (14, 15). For example, Fe–Mn spinel oxides have been found to activate PMS for decontamination via both radical (16–20) and direct electron transfer pathways (21) despite the similar catalyst composition. In addition, they generally show much lower nonradical catalytic activity than single-atom catalysts. Therefore, bimetal spinel oxides are promising for nonradical PMS catalysis, but such potential has been largely unexploited so far due to poor knowledge of the origin of their catalytic activity and selectivity.

One major barrier to mechanical study of bimetal spinel oxides lies in their compositional and structural complexity, which features a random distribution of both metals on the crystal framework of different geometries. Earlier work has identified the octahedral (Oh) metal site as the major active center for various heterogeneous catalytic processes, from 5-hydroxymethylfurfural oxidation (22) and CO oxidation (23) to O_2 reduction (24) and PMS activation (25). Therefore, we hypothesize that a colocation of both active metals on the octahedral sites of spinel oxide, which may be realized by fine-tuning the spinel

Significance

Advanced oxidation processes based on Fenton-like catalysis have been a core decontamination technology to protect the aquatic environment. However, implementing such technologies in an economically affordable and environmentally benign way remains a big challenge which hinders their widespread application, especially in underdeveloped countries/regions. Nonradical catalysis for selective decontamination based on inexpensive transition metal oxides offers opportunities to address this challenge, but a rational design of such catalysts has been hindered by poor understanding of the complicated bimetallic synergism. Herein, we shed light on the origins of the synergistic catalytic activity and selectivity of Fe–Mn spinel oxide, based on which we created a spinel oxide with unprecedented nonradical activity and peroxymonosulfate utilization efficiency to favor practical environmental application.

[1]To whom correspondence may be addressed. Email: wwli@ustc.edu.cn.

geometry, might decrease the system complexity to allow us to better reveal their crystal structure–activity–selectivity correlations.

In this work, we synthesized a series of $ZnFe_{2-x}Mn_xO_4$ spinel oxides (x = 0 to 2.0) comprising exclusively Zn-occupied tetrahedra (Td) for structural modulation and Fe- and Mn-occupied octahedra as the major active unit for PMS catalysis (Fig. 1A). By systematically comparing the electronic structure and catalytic behaviors of these catalysts via both experimental analysis and theoretical calculation, we identified electron delocalization as the decisive factor defining the catalytic selectivity of Fe–Mn spinel oxides for PMS activation. Intriguingly, the strong superexchange electronic interaction between the edge-sharing Fe and Mn in the octahedra renders the $ZnFeMnO_4$ catalyst a high-degree electron delocalization at the Mn site to enable nearly 100% nonradical activation of PMS. Finally, the high activity, stability, and environmental robustness of the catalysts for selective decontamination were also demonstrated.

Results

Crystal Structural Characterization. We first examined the geometries of the synthesized $ZnFe_{2-x}Mn_xO_4$ spinel oxides.

The X-ray diffraction (XRD) patterns of all the materials show typical phase-pure spinel crystalline structures (*SI Appendix*, Fig. S1). Rietveld refinement analyses (Fig. 1B) confirm that Zn is preferentially fixed at Td sites while both Fe and Mn cations occupy the Oh sites (26). Here, the $ZnMn_2O_4$ exhibits obvious tetragonal geometry attributed to Jahn–Teller distortion of high-spin Mn^{III} ($t_{2g}^3e_g^1$) in its spinel Oh sites and hence an elongated Mn–O bond along the z axis (*SI Appendix*, Table S1) (27, 28). With raised Mn content in the spinel the lengths of the Zn–O and Fe–O bonds decrease slightly (*SI Appendix*, Tables S2 and S3), as evidenced by the blue shift of Zn–O (540 to 625 cm^{-1}) and Fe/Mn–O (415 to 515 cm^{-1}) peaks in Fourier transform infrared (FTIR) spectra (*SI Appendix*, Fig. S2). The XRD peaks show high-angle shift with raised Mn content (*SI Appendix*, Fig. S1 and Table S4), indicating a primarily high-spin state of Fe cations at the Oh site (29). Nevertheless, all the $ZnFe_{2-x}Mn_xO_4$ spinel oxides show similar irregular shape and particle sizes (10 to 30 nm in diameter) except for $ZnFe_2O_4$, which exhibits obviously denser structure and larger sizes (1 to 2 µm in diameter) (*SI Appendix*, Fig. S3) and accordingly much smaller specific surface area (Fig. 1C). A closer observation by high-resolution transmission electron microscopy (HRTEM) in combination with selected-area
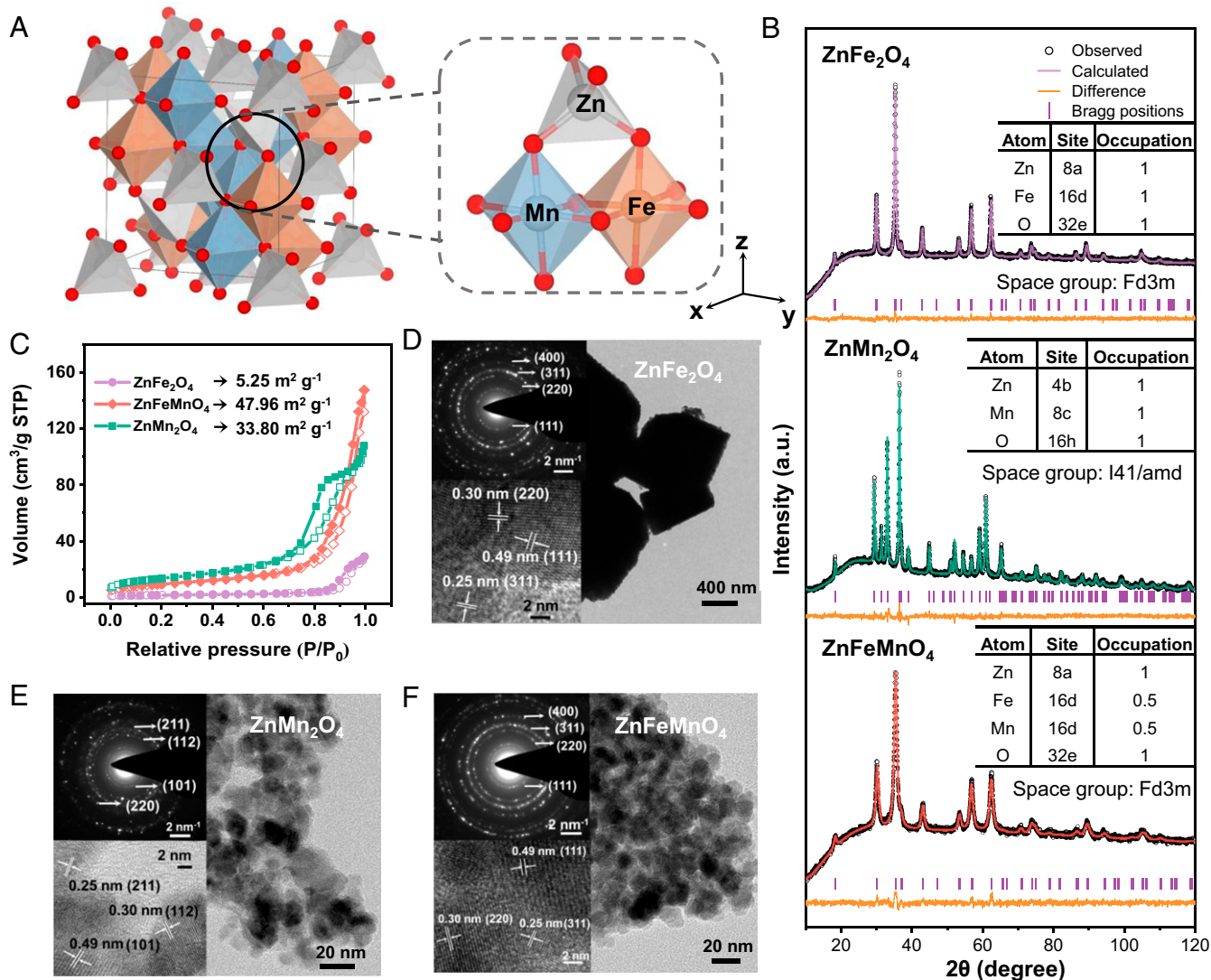

Fig. 1. Crystal structure and morphology of the $ZnFe_{2-x}Mn_xO_4$ spinel oxides. (A) Crystal structure of $ZnFeMnO_4$. (B) Rietveld refined XRD patterns, (C) BET surface areas, and (D–F) HRTEM and SAED images of different catalysts.

electron diffraction (SAED) and energy-dispersive X-ray spectroscopy analysis shows random orientation and polycrystalline character of the $ZnFe_{2-x}Mn_xO_4$ samples (Fig. 1 *D* and *F*) with evenly distributed constituent elements (*SI Appendix*, Fig. S4). Altogether, these results indicate a successful synthesis of a series of $ZnFe_{2-x}Mn_xO_4$ spinel oxides with the Td center exclusively occupied by inactive Zn cations, thus leaving abundant active Fe/Mn cations at the Oh sites to allow a systematic investigation into their synergic catalysis .

Catalytic Activities and Pathways of $ZnFe_{2-x}Mn_xO_4$. Interestingly, the $ZnFe_{2-x}Mn_xO_4$ (x = 0 to 2.0) catalysts differ substantially in their activities for PMS activation and bisphenol A (BPA) degradation despite their similar crystal structure. The $ZnFeMnO_4$ (x = 1) stands out as the most active one (Fig. 2*A*), achieving the highest BPA degradation kinetics (rate constant of ~0.43 min^{-1}) and mineralization degree (84% total organic carbon [TOC] removal within 15 min) (*SI Appendix,* Fig. S5). After normalizing to the Brunauer−Emmett−Teller (BET) surface area and dosage of the catalyst, the $ZnFeMnO_4$ still showed the highest specific activity for BPA degradation (kinetic constant of 0.09 $L\cdot min^{-1}\cdot m^{-2}$), far outperforming most of the reported binary transition metal oxides under similar conditions (*SI Appendix,* Table S5). Notably, it also delivers much higher activity than the individual or physically mixed single-metal oxides (Fig. 2*B*), suggesting a strong interplay between the Fe and Mn constituents in $ZnFeMnO_4$ spinel oxide. Such Fe–Mn synergy was obviously enhanced when the Fe and Mn were precisely confined at the Oh site of the spinel (i.e., $ZnFeMnO_4$) rather than randomly distributed in both the Td and Oh sites (i.e., $MnFe_2O_4$) (*SI Appendix,* Fig. S6). In addition, the significantly accelerated pollutant removal by the

$ZnFeMnO_4$/PMS system against the $ZnFeMnO_4$ or PMS alone (*SI Appendix,* Fig. S7) confirms the dominance of the Fenton-like catalytic process.

Besides the discrepant catalytic activities for PMS activation, the $ZnFe_{2-x}Mn_xO_4$ with different Fe/Mn ratios also varied in catalytic pathways. The results of quenching tests with different radical scavengers (ethanol for eliminating •OH and $SO_4^{•-}$, tertiary butyl alcohol for •OH) indicates a considerable generation of •OH and $SO_4^{•-}$ in both the $ZnMn_2O_4$ and $ZnFe_2O_4$ group but not in the $ZnFeMnO_4$ group (Fig. 2*C*). L-histidine addition caused no suppression in all three systems, indicating $^1O_2$ was not generated. Consistently, the electron paramagnetic resonance (EPR) analysis showed no signal of DMPO•-OH, DMPO•-SO₄, or TEMP-$^1O_2$ for $ZnFeMnO_4$ and $ZnMn_2O_4$ and showed only a weak DMPO•-OH signal for $ZnFe_2O_4$ (Fig. 2*D*). Therefore, the slightly suppressed BPA-degradation activity of $ZnFeMnO_4$ by tertiary butyl alcohol scavenger (*SI Appendix*, Fig. S8) should be mainly due to raised solution viscosity and the masking effect instead of radical quenching (30, 31). In addition, adding hydrophobic phenol as a scavenger for surface-bound radicals (19) caused no appreciable activity suppression (with negligible phenol consumption) for all the catalysts (*SI Appendix,* Fig. S9), thus the involvement of surface-bound radicals can also be ruled out. Overall, these results together imply that the nonradical PMS activation pathway dominates in $ZnFeMnO_4$ catalysis and has a smaller contribution to the decontamination activity of $ZnMn_2O_4$, while the radical pathway becomes predominant in the $ZnFe_2O_4$ catalytic system.

The pathways of nonradical PMS activation for pollutant degradation can be generally categorized into $^1O_2$ generation, high-valent metal, surface-activated complex, and electron
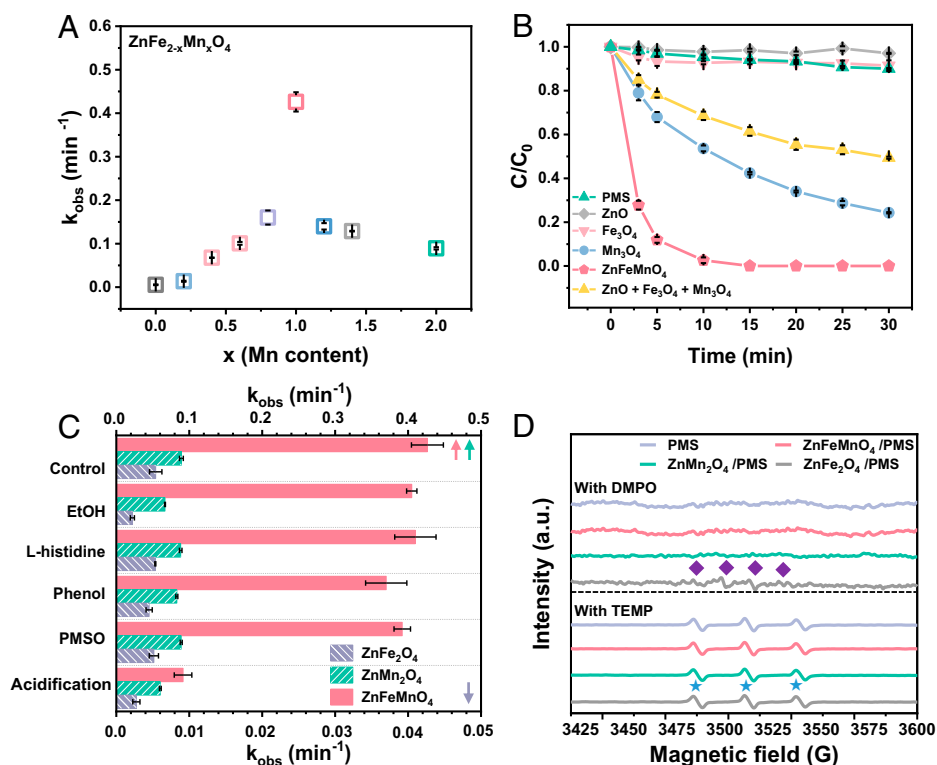

Fig. 2. Catalytic activity and pathway for PMS activation and BPA degradation. (*A*) Variations of catalytic activity of $ZnFe_{2-x}Mn_xO_4$ (x = 0 to 2.0) with Mn content. (*B*) BPA removal efficiency, (*C*) effects of different radical scavengers and acid pH on BPA degradation kinetics, and (*D*) EPR spectra of generated radicals in different catalyst/PMS systems. Reaction conditions for *A−C*: [BPA] = 10 $mg\cdot L^{-1}$, [PMS] = 0.05 $g\cdot L^{-1}$, [catalyst] = 0.1 $g\cdot L^{-1}$, if needed, [EtOH] = 8 mM, [L-histidine] = 0.16 mM, [phenol] = 10 mM, [PMSO] = 50 µM; for *D*, [DMPO] = 5 mM, [BPA] = 1 $mg\cdot L^{-1}$, [PMS] = 5 $mg\cdot L^{-1}$, [catalyst] = 10 $mg\cdot L^{-1}$, initial pH 6.0 (no buffer). a.u., arbitrary units.

transfer mediation mechanisms. Since the $^1O_2$ pathway has been ruled out in our reaction system, we further explored the other possible pathways. First, methyl phenyl sulfoxide (PMSO) was added to the ZnFeMnO$_4$/PMS system to probe high-valent Fe or Mn, but no obvious signal of methyl phenyl sulfone (PMSO$_2$) (32) was detected (Fig. 2C and *SI Appendix,* Fig. S10), indicating the absence of high-valent Fe or Mn species (33). The negligible contribution of high-valent Mn species to pollutant degradation is also supported by the fact that lowering the solution pH, which is supposed to stimulate the activity of high-valent Mn in Fenton-like catalysis, showed no promoting effect (Fig. 2C and *SI Appendix,* Fig. S11) (34). Therefore, the interfacial electron transfer pathways of electron transfer mediation and/or surface-activated PMS complex should be critically responsible for the BPA oxidation over ZnFeMnO$_4$.

These two interfacial electron transfer pathways are distinguished by the route of electron flow from the adsorbed pollutant to the surface-bound PMS, i.e., via direct interaction or through a conductive bridge of the catalyst (*SI Appendix,* Fig. S12). Notably, the electron transfer mediation pathway requires strong binding (i.e., inner-sphere adsorption) of both the organic and PMS on the catalyst surface. However, in our system, the ZnFeMnO$_4$ catalyst shows a much weaker binding affinity for BPA than PMS (adsorption energy of -0.85 eV vs. -3.91 eV), consistent with the limited adsorption of BPA detected (*SI Appendix,* Fig. S7A). The weak adsorption of BPA thus impedes its oxidation via electron transfer mediation. This is reasonable because such a pathway is generally more prone to occur in reaction systems with highly conductive materials (e.g., noble metals and carbons) rather than metal oxides (35). Therefore, BPA degradation in the ZnFeMnO$_4$/PMS system should be predominantly ascribed to the activity of the surface-activated PMS complex.

The formation of surface-activated PMS complex on ZnFeMnO$_4$ catalysts was verified by ionic strength test and in situ

Raman and FTIR spectral characterization. A distinct Raman peak at $\sim$836 cm^{-1} (corresponding to the PMS* complex) occurred upon PMS addition (Fig. 3A) and disappeared after BPA addition, indicative of the sequential processes of surface PMS* formation and consumption (10). In addition, the PMS decomposition process was highly pollutant-dependent: The PMS consumption within 30 min increased from 22% to 77% after BPA addition (Fig. 3B) and was not affected by radical scavengers (*SI Appendix,* Fig. S13), indicating a direct interaction between PMS* and BPA. The BPA degradation activity of the catalyst was not obviously affected by high ion concentration (100 mM NaClO$_4$) (*SI Appendix,* Fig. S14A), and the FTIR spectra show a slight red shift of the S–O peak of PMS (36) (at $\sim$617 cm^{-1}) upon catalyst addition (*SI Appendix,* Fig. S14B). All these results strongly support an inner-sphere complexation of PMS with the ZnFeMnO$_4$ surface, which results in surface-activated PMS* to directly extract electrons from BPA. Therefore, BPA is mainly oxidized by the surface-activated PMS* in the ZnFeMnO$_4$/PMS system (*SI Appendix,* Fig. S12B). Notably, the relatively weak adsorption of BPA does not impede its efficient oxidation on the catalyst surface, because it also favors easier desorption of the oxidation intermediates and leaves more binding sites for PMS* formation. This is supported by the poor correlation between the maximum adsorption capacity (Qe) and degradation rate (k$_{obs}$) of organic pollutants in the ZnFeMnO$_4$/PMS system (*SI Appendix,* Fig. S15) (37).

To clarify how PMS* interacts with BPA to enable its degradation, we next investigated the interfacial electron transfer process of the ZnFeMnO$_4$/PMS system by electrochemical assay. The amperometry i−t curves of the electrochemical system with catalyst-immobilized working electrode verify the formation of surface-activated PMS* on ZnFeMnO$_4$ (Fig. 3C). Specifically, it showed a sudden current drop (ΔI_{+PMS}) upon PMS addition and partial current rebounding (ΔI_{+BPA}) upon BPA dosage,
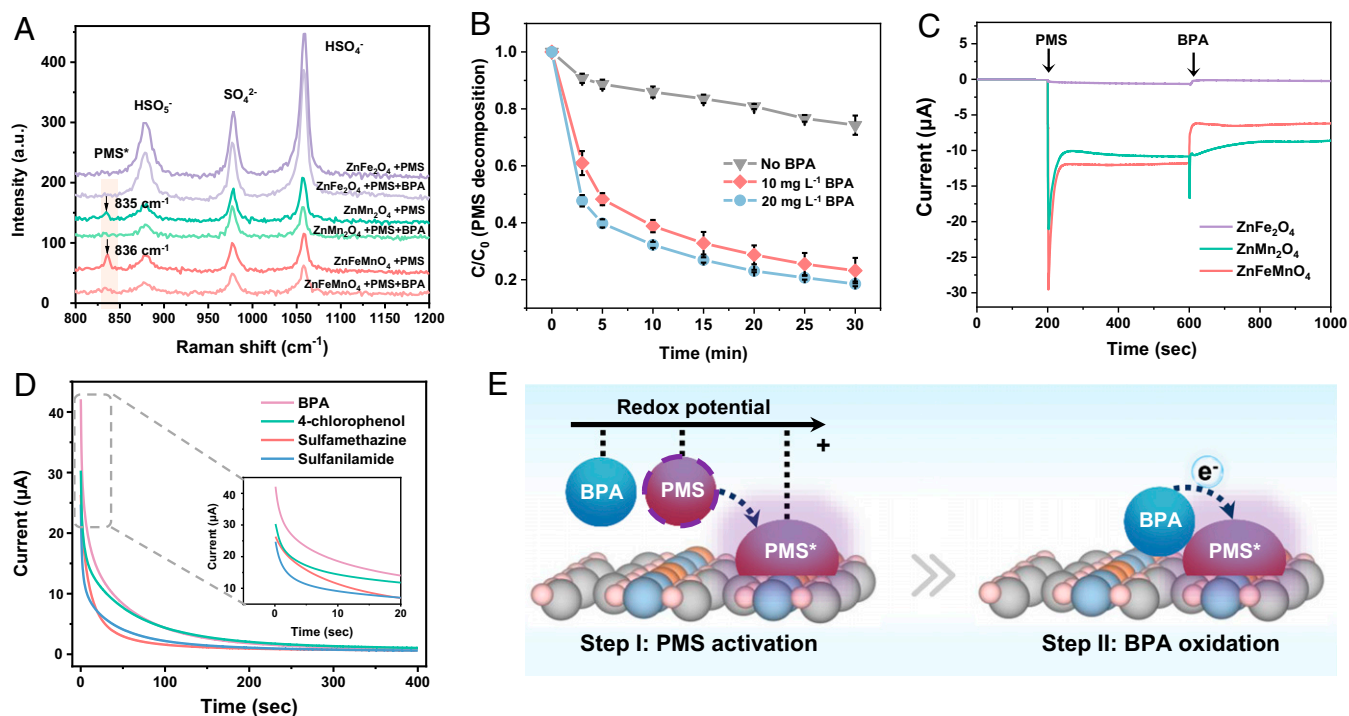
Fig. 3. Spectral and electrochemical properties of the catalysts in response to PMS and BPA addition. (A) In situ Raman spectra in ZnFe$_{2-x}$Mn$_x$O$_4$/PMS systems. a.u., arbitrary units. (B) PMS consumption with different BPA concentration. (C) I−t curves upon sequential addition of PMS and BPA. (D) I−t curves under 0.85-V potential of the ZnFeMnO$_4$ electrode with different pollutants. (E) Nonradical reaction mechanism of PMS activation and BPA oxidation ZnFeMnO$_4$ surface. Reaction conditions for B: [PMS] = 0.05 g·L^{-1}, [catalyst] = 0.1 g·L^{-1}, initial pH 6.0 (no buffer).

confirming a rapid formation and pollutant-related consumption of surface-bound PMS* (38–40). The ability of the surface-bound PMS* for direct oxidation of BPA was also evidenced by the higher open-circuit potentials of the ZnFeMnO$_4$/PMS (0.85 V) than the oxidation potential of BPA (0.60 V) (*SI Appendix*, Figs. S16 and S17). The direct oxidation mechanism was further supported by the preferential oxidation (reflected by the anodic current) of more electron-rich pollutants (BPA > 4-chlorophenol > sulfamethazine > sulfanilamide) (Fig. 3*D* and *SI Appendix*, Figs. S18 and S19) (41). Altogether, these results indicate an efficient electron transfer from electron-rich BPA to the adjacent PMS* complex on the ZnFeMnO$_4$ surface driven by potential difference, and thus highly efficient and selective degradation of BPA can be realized (Fig. 3*E*).

It should be noted that the surface-activated complex (PMS*) pathway was also identified for the other ZnFe$_{2-x}$Mn$_x$O$_4$ catalysts but had less contribution to their decontamination activities (Figs. 2 *C* and *D* and 3 *A* and *C* and *SI Appendix*, Fig. S16). According to the BPA degradation kinetics (Eqs. 2–7), this pathway accounts for about 93%, 66%, and 30% of the BPA degradation activity of the ZnFeMnO$_4$, ZnMn$_2$O$_4$, and ZnFe$_2$O$_4$ catalysts, respectively, revealing an obvious shift in catalytic pathway with the catalyst composition. To decipher what has caused such a catalytic pathway shift among the ZnFe$_{2-x}$Mn$_x$O$_4$ (x = 0, 1, 2) catalysts, we further explored the roles of the reactive metal species in the different spinel oxides. The superior PMS* pathway selectivity and high activity of ZnFeMnO$_4$ over ZnMn$_2$O$_4$ and ZnFe$_2$O$_4$ imply a strong synergistic interplay between the surface Fe$_{Oh}$ and Mn$_{Oh}$ components.

It is interesting to know how the catalytic properties of ZnFe$_{2-x}$Mn$_x$O$_4$ are regulated by the Fe–Mn interaction. We notice that surface-bound PMS*, indicated by the feature Raman peak at ∼836 cm^{-1}, was detected in both ZnFeMnO$_4$ and ZnMn$_2$O$_4$ but not in ZnFe$_2$O$_4$ (the Mn-free group) (Fig. 3*A*), signifying a plausibly critical role of surface Mn$_{Oh}$ in PMS* formation. However, previous studies suggest that Fe is typically a more preferential site over Mn for PMS adsorption (20). To clarify this contradiction, we performed density functional theory (DFT) calculation to examine the PMS binding affinity of different catalysts (Fig. 4 *A–C* and *SI Appendix*, Figs. S20 and S21). The results verify that PMS is indeed more prone to binding at the Fe$_{Oh}$ site of ZnFe$_2$O$_4$ than the Mn$_{Oh}$ site of ZnMn$_2$O$_4$. However, the situation changes when it comes to ZnFeMnO$_4$ that possesses both Fe$_{Oh}$ and Mn$_{Oh}$ sites. The PMS-binding affinity of Mn$_{Oh}$ was raised drastically from −2.25 eV to −3.91 eV in the presence of edge-sharing Fe$_{Oh}$, making it a more preferential PMS-binding site over Fe$_{Oh}$. In addition, the strong Fe–Mn interaction in ZnFeMnO$_4$ enables a moderate PMS adsorption strength compared with other catalysts (*SI Appendix*, Fig. S22), which is conducive to altering the charge density of the surface layer and even the deeper atoms of catalyst to improve its reactivity (40). Notably, the Mn site of ZnFeMnO$_4$ is also the predominant binding site for BPA. The ZnFeMnO$_4$ showed much weaker adsorption of BPA (−0.85 eV) in comparison with ZnMn$_2$O$_4$ (−1.37 eV) and ZnFe$_2$O$_4$ (−3.15 eV) (*SI Appendix*, Fig. S23), indicating that weak adsorption of BPA is beneficial for raising the catalytic activity and nonradical pathway selectivity of ZnFe$_{2-x}$Mn$_x$O$_4$ for PMS activation. Interestingly, we found that the PMS activation pathway of spinel oxides is highly associated with the competitive adsorption of BPA and PMS (*SI Appendix*, Fig. S24): Stronger adsorption of PMS paired with weaker adsorption of BPA favors the PMS* complex pathway, while the opposite favors the radical pathway. Thus, such a competitive adsorption

behavior lay the basis for the selective catalysis over the ZnFe$_{2-x}$Mn$_x$O$_4$ catalysts.

To further decipher the mechanisms of the Fe–Mn synergy that regulate the PMS binding and activation by ZnFe$_{2-x}$Mn$_x$O$_4$, we next examined the catalyst surface electronic properties, especially at the Mn$_{Oh}$ site which has been identified as the predominant reactive site of ZnFeMnO$_4$ for PMS binding and nonradical activation. The X-ray photoelectron spectra (XPS) of all the catalysts show two typical peaks of Zn 2p (∼1,044.3 eV and ∼1,021.2 eV) corresponding to tetrahedral Zn^{II} (*SI Appendix*, Fig. S25), which has fully occupied d orbitals [3d (10)] and hence cannot electronically interact with the corner-sharing Mn$_{Oh}$ or Fe$_{Oh}$ (24, 42). Previous studies suggest that surface oxygen group (O$_{ad}$, ∼531.2 eV) might also be able to active PMS. However, the O 1s XPS spectra identify minimum content of O$_{ad}$ in the most active catalyst of ZnFeMnO$_4$ (Fig. 4*D*). Apparently, the discrepant PMS activation performances of the ZnFe$_{2-x}$Mn$_x$O$_4$ catalysts are not ascribed to the Zn element or the surface-adsorbed oxygen species.

Notably, the Fe and Mn species in different catalysts vary substantially in their surface chemical states. The ZnFeMnO$_4$ has much less Fe^{III} content than ZnFe$_2$O$_4$ (Fe^{III}/Fe^{II} ratio of 2.03 vs. 2.95) (Fig. 4*E*) and higher Mn^{III} and Mn^{IV} contents than ZnMn$_2$O$_4$ (Fig. 4*F*). Such surface electronic redistribution is further verified by the soft X-ray absorption spectra (XAS) measurements of the 3d states of transition metals (TM) and their hybridization with the O 2p state. The results show that ZnFeMnO$_4$ and ZnFe$_2$O$_4$ possess a dominant amount of octahedral Fe^{III} species with signature doublets of both L_2 and L_3 edges (Fig. 4*G*). The higher intensity of the shoulder peak (∼707.2 eV) at the Fe-L_3 edge of ZnFeMnO$_4$ indicates that it has higher octahedral Fe^{II} content than the ZnFe$_2$O$_4$ counterpart (43), in agreement with XPS analyses. Moreover, the Mn-L_3 peak of ZnFeMnO$_4$ shows an obvious positive shift with broadened peak shape relative to that of ZnMn$_2$O$_4$ (Fig. 4*H*), suggesting the presence of more abundant Mn^{IV} species and delocalized Mn states in ZnFeMnO$_4$ (44). Notably, the significantly raised Mn^{IV} content coincides well with the improved electron affinity of Fe^{III} in ZnFeMnO$_4$, indicating that Fe–O–Mn superexchange interaction (Mn^{III} + Fe^{III} → Mn^{IV} + Fe^{II}) might occur in the spinel lattice. In addition, the O K-edge XAS spectra reveal different pre-edge (≤ 535 eV) of ZnFe$_{2-x}$Mn$_x$O$_4$ that features TM 3d-O 2p hybridization and t$_{2g}$–e$_g$ occupancy (Fig. 4*I*). The closest doublet intensities and the highest normalized percentage of the pre-edge peak (shaded area) confirm the delocalization of TM 3d states and their strong hybridization with O 2p (45). Overall, these evidences indicate the existence of strong Fe–O–Mn electronic interaction, as an important machinery of Fe–Mn synergic catalysis, in ZnFeMnO$_4$ to critically tune its catalytic properties. Specifically, such Fe$_{Oh}$–O–Mn$_{Oh}$ interaction may trigger electron hopping from the degenerated e$_g$ orbitals of Mn^{III} to the t$_{2g}$ orbitals of Fe^{III} through the edge-sharing octahedra network (Fig. 5*A*), thereby reconstructing the Fe/Mn electronic states in ZnFeMnO$_4$ relative to those in ZnFeMnO$_4$ and ZnMn$_2$O$_4$. The Mn^{III} can also be replenished from Mn^{II} via reacting with the more electron-affinitive Fe^{III} (Mn^{II} + Fe^{III} → Mn^{III} + Fe^{II}) to sustain the Fe–Mn superexchange interaction, which strengthens the surface binding and nonradical activation of PMS. Similar electronic structure modulation and activity improvement induced by bimetallic electronic exchange interaction have also been found in Co–Mn spinel oxide for oxygen reduction reaction catalysis and Ni–Co spinel oxide for oxygen evolution reaction catalysis (24, 46).
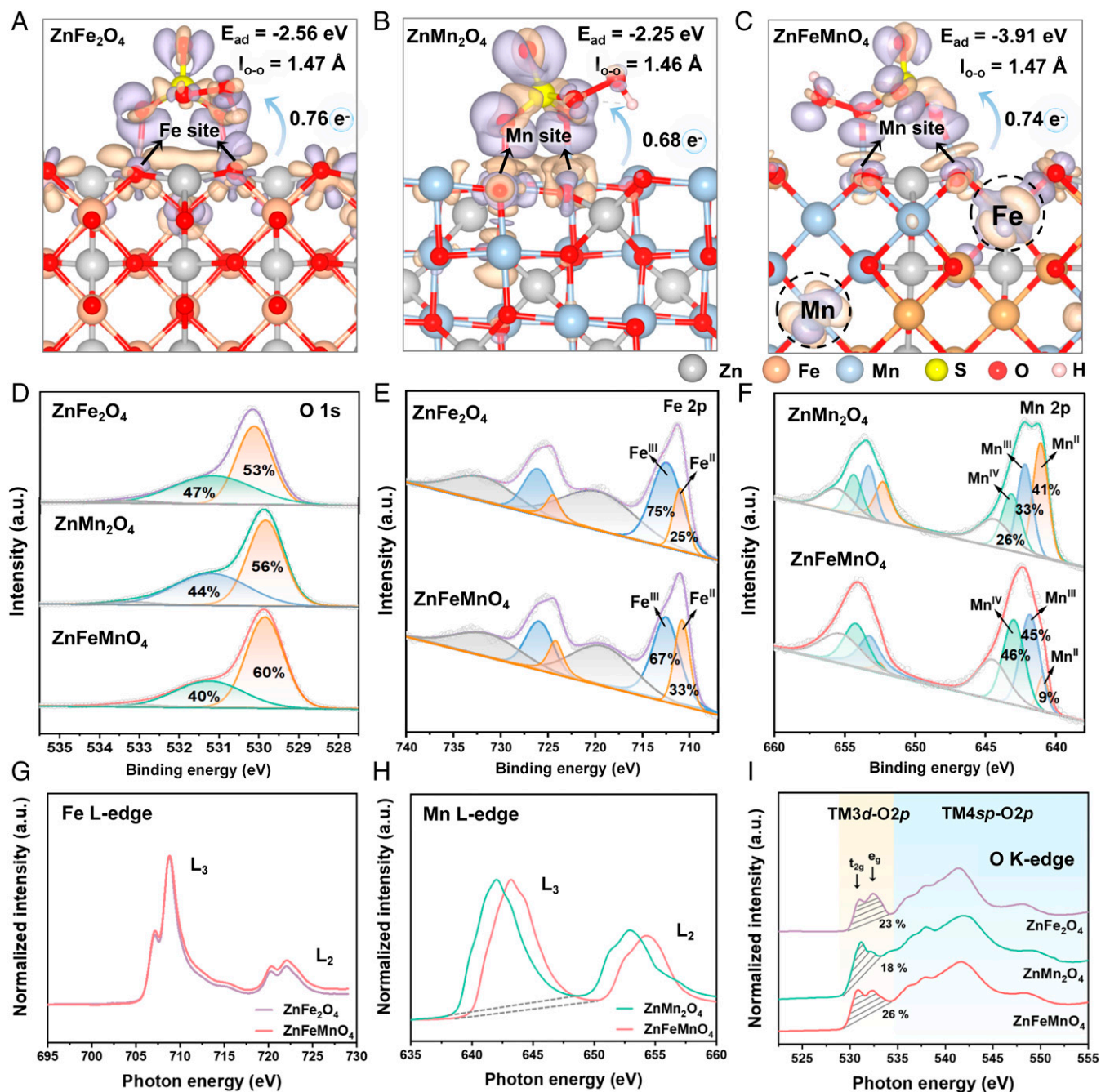
Fig. 4. Electronic structure and PMS-binding properties of $ZnFe_{2-x}Mn_xO_4$. (*A–C*) Charge density difference ($\rho_{total} - \rho_{substrate} - \rho_{PMS}$) in optimized configurations of $ZnFe_{2-x}Mn_xO_4$ (110)/PMS systems estimated by DFT calculation. The O–O bond length of PMS and the number of charge transfers from catalysts to PMS are indicated on the configurations. The isosurface contour is 0.003 e/bohr (3). The light purple and light orange denote the electron accumulation and electron depletion, respectively. (*D–F*) XPS spectra of O 1s, Fe 2p, and Mn 2p of the $ZnFe_{2-x}Mn_xO_4$. a.u., arbitrary units. (*G–I*) Normalized XAS spectra at the Fe *L*-edge, Mn *L*-edge, and O *K*-edge of different catalysts recorded in total electron yield (TEY) mode at room temperature.

Fe–Mn Synergic Catalysis Machinery of ZnFeMnO₄. The molecular machinery of activity enhancement and pathway regulation of $ZnFe_{2-x}Mn_xO_4$ via Fe–Mn superexchange interaction is further unveiled by DFT calculation. Since the Fe–Mn superexchange is mediated by the lattice oxygen in the spinel oxides, the interaction should be critically affected by the orbital coupling between Fe/Mn 3d and O 2p. Analysis of the surface projected density of states (PDOS) in ZnFeMnO₄ (*SI Appendix,* Fig. S26) shows a high-degree overlap between the Mn_{Oh} 3d and O 2p orbitals and a moderate overlap between the Fe_{Oh} 3d and O 2p orbitals, consistent with the more important catalytic role of the Mn_{Oh} over Fe_{Oh} sites identified above. The stronger overlap between Mn_{Oh} 3d and O 2p orbitals in ZnFeMnO₄ than in ZnMn₂O₄, consistent with the higher activity of ZnFeMnO₄, further supports a pivotal role of the Mn_{Oh} sites in PMS activation. The highly overlapped Mn 3d and O 2p orbitals in ZnFeMnO₄ thus enable efficient Fe–Mn superexchange interaction, resulting in obvious valence redistribution of the Fe and Mn species (indicated by the calculated Bader charge and the corresponding XPS results) relative to the other catalysts (Fig. 5*B*). The creation of more Mn^{IV} ($t_{2g}^3 e_g^0$) on the catalyst surface (*SI Appendix,* Table S6) renders ZnFeMnO₄ abundant zero-filling e_g orbitals to strongly adsorb and activate PMS (25). Analysis of the orbital states near the Fermi level
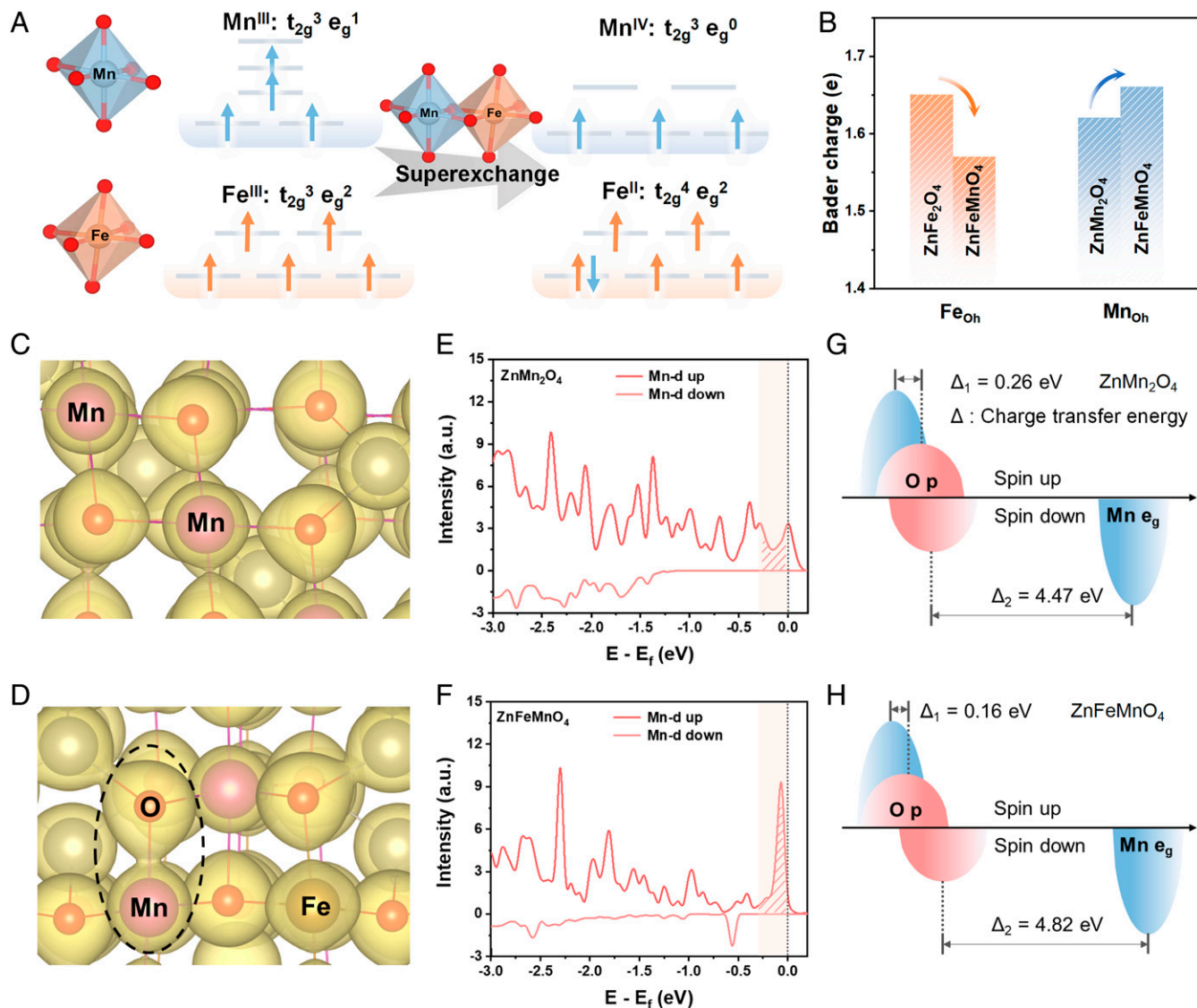
Fig. 5. Electronic delocalization at the catalyst surface for promoting nonradical PMS activation. (*A*) Schematic illustration of superexchange interaction and e_g occupancy of Fe_{Oh} and Mn_{Oh} in $ZnFeMnO_4$. (*B*) Computed bader charges of Fe_{Oh} and Mn_{Oh} in $ZnFe_{2-x}Mn_xO_4$ oxides. The corresponding charge-density wave of (*C*) $ZnMn_2O_4$ and (*D*) $ZnFeMnO_4$, respectively. The density of states of (*E*) $ZnMn_2O_4$ (110) and (*F*) $ZnFeMnO_4$ (110) surfaces. a.u., arbitrary units. Schematic representation of the Mn e_g and O p-band centers for (*G*) $ZnMn_2O_4$ (110) and (*H*) $ZnFeMnO_4$ (110) surfaces.

also confirms that $ZnFeMnO_4$ is more prone to exchange electrons with PMS than $ZnFe_2O_4$ and $ZnMn_2O_4$ (47). Therefore, the Fe–Mn superexchange interaction significantly alters the e_g occupancy of Mn species, an important indicator of the catalyst electronic structure. Such superexchange-induced electronic structure change of the catalyst does not affect the interfacial electron transfer number and structure of the surface-bound PMS* (shown by the similar O–O bond length for $ZnFeMnO_4$ and $ZnMn_2O_4$), which typically change in radical-based PMS activation processes (Fig. 4 *A–C*).

The charge density analysis reveals that the highly unoccupied e_g states of Mn_{Oh} in $ZnFeMnO_4$ trigger electron delocalization at the Mn_{Oh} site at a much higher degree than that in $ZnMn_2O_4$ (Fig. 5 *C* and *D*). Accordingly, the surface Mn_{Oh} atoms of $ZnFeMnO_4$ show increased PDOS from ~0.30 eV to the Fermi level (the shaded part in Fig. 5 *E* and *F*) relative to those in $ZnMn_2O_4$, owing to the delocalized electrons (48, 49). This renders the $ZnFeMnO_4$ higher electronic conductivity than the other catalysts, as evidenced by its smallest charge-transfer resistance (50) (*SI Appendix*, Fig. S27). Also

benefited from the strong Fe_{Oh}–O–Mn_{Oh} superexchange interaction, $ZnFeMnO_4$ shows lower energy difference (~0. 16 eV) between the spin-up Mn_{Oh} e_g and O p-band centers relative to other catalysts (Fig. 5 *G* and *H* and *SI Appendix*, Fig. S28 and Tables S7 and S8). Therefore, the electron delocalization of $ZnFeMnO_4$ endows it with high conductivity and low energy barrier to facilitate binding and nonradical activation of PMS. Similar correlations between the electrical conductivity, activity, and electron delocalization level of metal materials have also been found in other catalytic systems(9, 46). Based on the above analyses, we can conclude that the PMS activation pathway and activity of Fe–Mn spinel oxide are profoundly regulated by the Fe–Mn synergisms: The Fe–Mn superexchange interaction through the O edge-sharing octahedra of $ZnFeMnO_4$ enables a strong electron delocalization at the surface Mn_{Oh} site, rendering it high PMS-binding affinity and superior electron conductivity to facilitate nonradical activation of PMS. This might be an important origin of the catalytic activity for nonradical PMS activation over bimetallic spinel oxides.

Performance of ZnFeMnO₄ for Practical Decontamination Application. Attributed to the unique Fe–Mn synergy, the ZnFeMnO₄ catalyst exhibits extraordinary activity for PMS activation, enabling much fast BPA degradation at less PMS dosage than most nonradical catalysts including the benchmark Co_3O_4 (Fig. 6*A* and *SI Appendix*, Fig. S29 and Table S5). The catalyst also exhibits superior stability for cyclic BPA degradation, achieving 100% BPA removal within 15 min in the first three cycles (Fig. 6*B*). Although the BPA removal ratio declined to 90% in the fifth cycle, the catalyst showed no appreciable change in crystalline structure and electronic states after the cyclic reaction (*SI Appendix*, Fig. S30). The metal leaching was also negligible; the average leaching ratios of Zn, Fe, and Mn ions were only 0.43%, 0.20%, and 0.31%, respectively (*SI Appendix*, Table S9). These results indicate a good stability of the ZnFeMnO₄ catalyst, owing to its chemically stable spinel structure and the appropriate reaction conditions, i.e., weak acidic pH due to low PMS dosage (*SI Appendix*, Fig. S31*A*) and mild oxidative condition due to the absence of aggressive radicals. The homogeneous catalytic system constructed by adding the same amount of leached metal ions or directly using the leaching solution (without catalyst) showed negligible BPA degradation (*SI Appendix*, Fig. S31*B*), confirming the dominance of Fenton-like catalysis in the ZnFeMnO₄/PMS system.

Given the high chemical stability of ZnFeMnO₄, its slight activity decline during the cyclic BPA degradation should be mainly attributed to an accumulation of oxidation intermediates on the catalyst surface. The FTIR spectra confirm the formation of aromatic compounds from BPA oxidation on the catalyst surface in the ZnFeMnO₄/PMS system (*SI Appendix*, Fig. S32) (20, 51). Nevertheless, such aromatic intermediates can be easily removed and the catalyst activity can be fully restored by simple thermal treatment (heating at 300 °C for 1 h in the air) or chemical elution (with ethanol for 1 h) (Fig. 6*B* and *SI Appendix*, Fig. S33). In addition, it is noteworthy that our reaction system consumes much less PMS (0.08 mM) than most heterogeneous Fenton-like reaction systems (typically above 0.33 mM), with the PMS utilization ratio (up to ∼82%) surpassing all the reported heterogeneous catalysts (*SI Appendix*, Table S5). Such a high PMS utilization ratio is beneficial for water pollution control due to decreased treatment cost and less generation of undesirable sulfate products in the effluent.

The nonradical PMS activation pathway with exclusively surface-bound PMS* complex for pollutant degradation also renders the ZnFeMnO₄ catalyst superior resistance to pH variation, high salinity, and environmental interferences. It maintained high catalytic activity (almost 100% BPA degradation within 30 min) in the broad pH range of 3.5 to 9.5 (*SI Appendix*, Fig. S34*A*), where the slight performance decline at alkaline pH should be attributed to electrostatic repulsion between the negatively charged catalyst and PMS (*SI Appendix*, Fig. S34*B*). Even under ultrahigh salinity conditions (50 to 200 mM) with various inorganic anions (i.e., Cl^-, NO_3^-, HCO_3^-, and SO_4^{2-}), a high activity of the catalyst (>80% BPA degradation within 30 min) still remained (*SI Appendix*, Fig. S35). In addition, it also exhibited amazing catalytic activity for treating tap water, lake water, and real electroplating tail wastewater (electrical conductivity ∼1.7 S/m), achieving >96% BPA removal within 15 min in all these cases (*SI Appendix*, Fig. S36). Finally, we built a fixed-bed column reactor (1-L working volume), with ZnFeMnO₄ catalyst immobilized on polyester fiber ball carriers, to test its performance for continuous water decontamination under a hydraulic retention time of ∼13.3 min (Fig. 6 *C* and *D*). The fiber ball carriers possess superior wettability and high porosity (*SI Appendix*, Fig. S37) to favor sufficient water dispersion. This ZnFeMnO₄-fiber ball/PMS
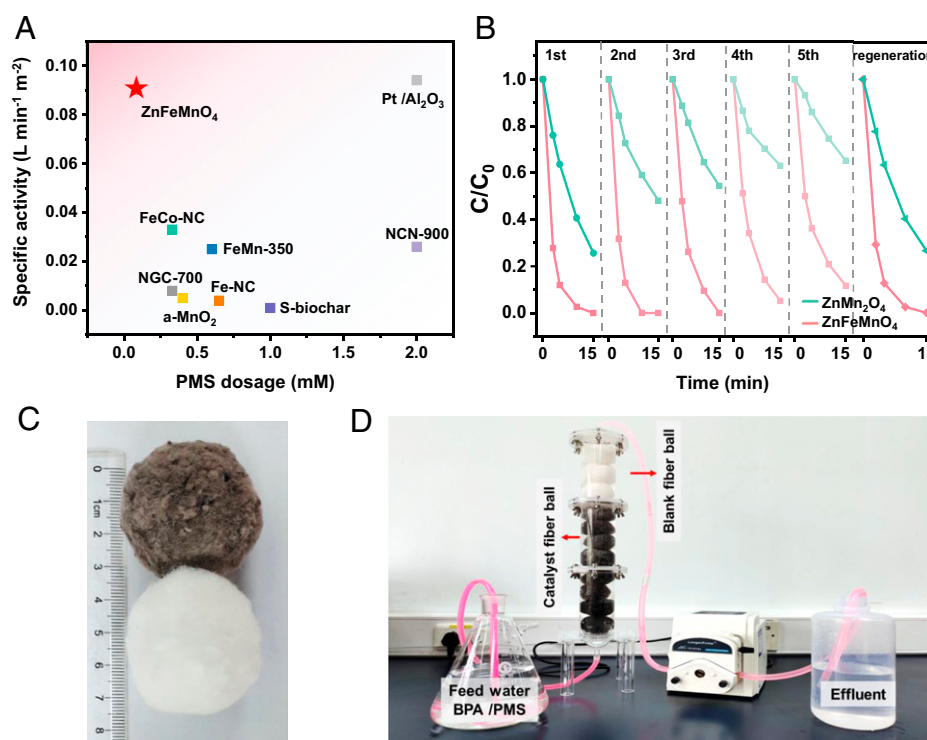

Fig. 6. PMS utilization efficiency and stability of ZnFeMnO₄ for BPA degradation. (*A*) Comparison of intrinsic catalytic activity of the ZnFeMnO₄ with the reported catalysts in literature for nonradical PMS activation. (*B*) Cyclic BPA removal performances of different catalyst/PMS systems. (*C*) Polyester fiber balls loaded with/without ZnFeMnO₄ catalyst. (*D*) A home-made column reactor for treatment of BPA-containing water. Reaction conditions for *B*: [BPA] = 10 mg·L⁻¹, [PMS] = 0.05 g·L⁻¹, [catalyst] = 0.1 g·L⁻¹, initial pH 6.0 (no buffer). Reaction conditions for *D*: [BPA] = 10 mg·L⁻¹, [PMS] = 0.05 g·L⁻¹, [catalyst] = 80 mg, flow rate = 50 mL·min⁻¹, initial pH 6.0 (no buffer).

system under up-flow operating mode showed a stable treatment performance with 92.7% BPA removal during continuous operation. In addition, it achieved high turnover number of ~547 and turnover frequency of ~8.2 for treating 5-L BPA-containing water, implying a great potential for practical water decontamination application.

Discussion

We developed a series of $ZnFe_{2-x}Mn_xO_4$ spinel oxides for PMS activation, identified the key material properties governing the catalytic pathway and activity, and elucidated the underlying Fe–Mn synergism. $ZnFeMnO_4$ serves as an ideal model for probing into the structure–activity correlations of spinel oxide catalysts due to its flexible tunability in crystal geometry and surface chemistry (52). In addition, the high catalytic activity and selectivity, low cost, and environmental benignity of $ZnFeMnO_4$ also make it highly attractive for practical environmental application. Interestingly, the $ZnFeMnO_4$ with exclusively Zn-occupied tetrahedra and Fe- and Mn-occupied octahedra allows a strong superexchange interaction between the edge-sharing $[FeO_6]$ and $[MnO_6]$. Such an unusual Fe–Mn interaction induces electron delocalization at the surface Mn_{Oh} site to boost PMS adsorption and interfacial charge transfer, thus favoring a nonradical activation of PMS via forming surface-bound PMS* complex. The $ZnFeMnO_4$ exhibited extraordinary intrinsic activity and much less PMS consumption than all the reported nonradical heterogeneous catalysts and maintained high catalytic activity under broad pH, high salinity, and real water matrix conditions, implying a great potential for water decontamination application.

Notably, although the good performance of the $ZnFeMnO_4$ catalyst has been demonstrated, there is still plenty of room for further improvement of such spinel oxides (e.g., in composition, crystal structure, and morphology) to facilitate their practical application. For example, other alternative transition metals may be considered (53) and the metal occupation in the spinel lattice, especially at the active Oh sites, can be fine-tuned by changing the synthesis temperature or other operating conditions (54). In addition, the pollutant degradation activity of the spinel oxides may be further improved by morphology engineering or loading the catalyst on appropriate support materials (55), which may not only increase the reactive surface area and enable selective adsorption of target pollutants but also induce confined catalysis or create unique electronic metal-support interaction to facilitate interfacial catalysis (56). Overall, there are tremendous opportunities for polymetal spinel oxides in Fenton-like catalysis, although considerable challenges remain that hinder a rational design of such catalysts. Overcoming these hurdles necessitates a deep understanding of the structure–activity relationships and the metallic synergy at both microscopic and macroscopic levels, which warrant future investigations.

In summary, our work provides fundamental insights into the Fenton-like catalysis over Fe–Mn spinel oxides and opens a new avenue for modulating the catalytic selectivity of such bimetallic spinel oxide materials. The findings here may lay an important basis to guide a rational design of mixed-metal heterogeneous catalysts for efficient and selective water decontamination processes. Importantly, it is reasonable to expect that such electronic exchange interactions might widely exist in a broad range of mixed metal oxides and fundamentally affect their catalytic behavior, which remain to be clarified. In addition, although we focus on PMS activation, the regulation strategies for modulating the catalytic selectivity of metal oxides might be readily extended to other catalytic systems, such as water oxidation and chemical synthesis, thus motivating new advances in sustainable energy and chemical production technologies (57–59).

Methods

Chemicals and Materials. All chemicals and reagents were of analytical grade and used without further purification. PMS ($2KHSO_5·KHSO_4·K_2SO_4$, 4.5% active oxygen) was purchased from Beijing J&K Co., Ltd. Nanoscale oxides of Mn_3O_4, Fe_3O_4, ZnO, and Co_3O_4 and $Zn(C_5H_7O_2)_2$, $Fe(C_5H_7O_2)_3$, and $Mn(C_5H_7O_2)_3$ chemicals were obtained from Shanghai Macklin Biochemical Co., Ltd. Mobile phase (gradient-grade methanol and acetonitrile) and spin trapping reagents (5,5-dimethyl-1-pyrroline-N-oxide [DMPO] and 2,2,6,6-tetramethyl-4-piperidone [TEMP]) were purchased from Sigma-Aldrich. Other chemicals and materials were purchased from Sinopharm Chemical Reagent Co., Ltd.

Catalyst Preparation. $ZnFe_{2-x}Mn_xO_4$ spinel oxides (x = 0 to 2.0) were synthesized via a two-step reaction. For a typical synthesis, 0.3 g polyvinylpyrrolidone (molecular weight = ~58,000 g/mol) was dissolved in 150 mL ethylene glycol. After the solution became transparent, $Zn(C_5H_7O_2)_2$, $Fe(C_5H_7O_2)_3$, and $Mn(C_5H_7O_2)_3$ at desired molar ratios were dissolved in the above solution under vigorous stirring at room temperature for 2 h. Subsequently, the mixture was maintained at 190 °C in oil bath for 6 h. The formed precipitate was centrifuged and washed with ethanol to remove the unreacted reactants. The samples were dried in an oven at 60 °C overnight and subsequently calcined at 500 °C for 3 h in the air at a heating rate of 3 °C·min^{-1} to yield the final products. $MnFe_2O_4$ spinel oxide was fabricated via the same procedures as $ZnFe_{2-x}Mn_xO_4$ except for not adding $Zn(C_5H_7O_2)_2$ addition.

Commercial metal oxides catalysts of ZnO, Fe_3O_4, Mn_3O_4, and Co_3O_4 powder were also used as controls without any further purification.

Catalyst Characterization. The crystal structures of the synthesized $ZnFe_{2-x}Mn_xO_4$ catalysts were examined by XRD using a Rigaku Miniflex-600 diffractometer operated at 40 kV and 15 mA with Cu Kα radiation (λ = 1.5406 Å). Rietveld refinement of the XRD data was conducted using GSAS software (60). The x value in $ZnFe_{2-x}Mn_xO_4$ structural formulae was determined by the atomic ratios of Zn, Fe, and Mn in the samples analyzed by inductively coupled plasma-atomic emission spectroscopy (Optima 7300 DV; PerkinElmer Inc.). These measured values can better reflect the true composition of the catalysts than the estimates based on regular dosage (*SI Appendix*, Table S10). The material morphologies were observed by field emission scanning electron microscopy (FEI Quanta FEG-250) and TEM (Hitachi H7700) at an acceleration voltage of 100 kV. The BET specific surface areas of the catalysts were measured by N_2 adsorption−desorption method on a Builder 4200 instrument. The surface chemical characteristics of the catalysts were analyzed by XPS on a Thermo ESCA-LAB 250 analyzer equipped with an Al Kα (hv = 1,486.6 eV) X-ray source. The binding energy was calibrated with the C 1s peak at 284.8 eV. Zeta potential of the catalysts was recorded by Zeta sizer (Nano). FTIR spectroscopy spectra were collected by IR microscopy (NicoletiN10, Thermo Fisher Inc.). In situ Raman spectra were monitored on a Raman spectrometer (Horiba Scientific) with a green laser at 532 nm.

Evaluation and Analytical Methods of Catalytic Activity. Unless otherwise specified, the degradation experiments were carried out in 20 mL pollutant solution (10 mg·L^{-1} BPA as the model) at room temperature (25 ± 2 °C). After adding catalyst (2 mg) into the BPA solution, ultrasonic dispersion (1 min) and magnetic stirring (15 min) were immediately applied to ensure uniform suspension and sufficient adsorption−desorption equilibrium of the catalyst. Then, PMS (1 mg) was added to initiate the reaction. The reaction sample was collected at given time intervals and mixed immediately with sodium sulfite to cease the reaction. After filtration through 0.22-μm cellulose ester membranes, the samples were subjected to concentration measurements. All the experiments were carried out in duplicate or triplicate.

The initial pH values (before PMS addition) of the reaction solutions were adjusted with 0.1 M NaOH or HCl. The chemical stability of the catalysts was evaluated based on the BPA degradation performances in five consecutive reaction cycles. After each cycle, the catalysts were recovered by centrifugation, washed with deionized water twice, and then reused without drying.

The BPA concentration was measured by high-performance liquid chromatography (6460; Agilent Inc.) with a Kromasil C18 column (4.6 × 250 mm, 5 μm) at a detection wavelength of 273 nm. A mixture of acetonitrile/formic acid (0.1%) (40:60, vol/vol) at a flow rate of 1 mL·min^{-1} was used as the mobile phase. Similarly, the PMS concentration was analyzed by a ultraviolet-visible spectrometer (1600; Mapada) (61). Generally, 100 μL standard solution or sample was added into 10 mL mixed solution of 0.05 M KHCO$_3$ and 0.24 M KI. The subsequent solution was shaken immediately and then analyzed at 352 nm after reacting for 15 min. The DMPO and TEMP were employed as the spin-trapping agent to capture SO$_4^{\bullet-}$/•OH and $^1O_2$, respectively. The corresponding signals were detected using an EPR Bruker ER200-SRC spectrometer. The TOC concentration was determined by a Shimadzu TOC-VCPH analyzer. The leached Zn, Fe, and Mn ions after the reaction were determined by inductively coupled plasma mass spectrometry. The BPA degradation rates were calculated according to the pseudo-first-order kinetic model (Eq. **1**)

$$-\ln\left(\frac{C_t}{C_0}\right) = k_{obs} \cdot t, \qquad [1]$$

where C_t is the BPA concentration at a certain reaction time (t) and C_0 is the initial BPA concentration (after reaching adsorption−desorption equilibrium); k_{obs} is the apparent rate constant. We further quantified the contributions of •OH, SO$_4^{\bullet-}$, $^1O_2$, surface-bound •OH and SO$_4^{\bullet-}$, Fe^{IV}, and Mn^{IV} for the BPA degradation. The apparent rate constants with EtOH, L-histidine, phenol, PMSO addition, or at initial acid condition were determined as k_1, k_2, k_3, k_4, and k_5, respectively, and the rate constant of the group without scavengers was k_0. Thus, the fraction of BPA degradation contributed by the above species and by direct oxidation at catalyst surface were calculated according to Eqs. **2**–**7** (13):

$$\lambda(\bullet OH \text{ and } SO_4^{\bullet-}) = (k_0 - k_1)/k_0 \qquad [2]$$

$$\lambda(^1O_2) = (k_0 - k_2)/k_0 \qquad [3]$$

$$\lambda(\text{surface} - \text{bound } \bullet OH \text{ and } SO_4^{\bullet-}) = (k_0 - k_3)/k_0 \qquad [4]$$

$$\lambda(Fe^{IV}) = (k_0 - k_4)/k_0 \qquad [5]$$

$$\lambda(Mn^{IV}) = (k_0 - k_5)/k_0 \qquad [6]$$

$$\lambda(\text{direct oxidation}) = 1 - \lambda(\bullet OH \text{ and } SO_4^{\bullet-}) - \lambda(^1O_2) - \lambda(\text{surface} - \text{bound } \bullet OH \text{ and } SO_4^{\bullet-}) - \lambda(Fe^{IV}) - \lambda(Mn^{IV}), \qquad [7]$$

where λ (•OH and SO$_4^{\bullet-}$), λ ($^1O_2$), λ (surface-bound •OH and SO$_4^{\bullet-}$), λ (Fe^{IV}), λ (Mn^{IV}), and λ (direct oxidation) were the contribution of •OH and SO$_4^{\bullet-}$, $^1O_2$, surface-bound •OH and SO$_4^{\bullet-}$, Fe^{IV}, Mn^{IV}, and the direct oxidation mechanism to the BPA degradation, respectively.

Electrochemical assays were all performed in a three-electrode cell connected to a CHI (760E) workstation, with a catalyst-modified glassy carbon electrode as the working electrode, a platinum wire as the counterelectrode, and Ag/AgCl electrode as the reference electrode. To prepare the working electrode, the catalyst ink was fabricated by ultrasonically mixing 2 mg of the catalyst, 0.24 mL of Millipore Q H$_2$O (15 MU), 0.74 mL of isopropyl alcohol, and 0.02 mL of 5 wt % Nafion dispersion solution. Then, 10 μL ink was drop-casted on a freshly polished glassy carbon electrode, which corresponds to a catalyst loading amount of 0.1 mg·cm^{-2} disk. Na$_2$SO$_4$ (50 mM) solution was used as the electrolyte. Chronoamperometry analyses were carried out at the bias of the system's open-circuit voltage. In order to obtain appreciable current values, PMS and BPA samples were added into the electrolyte at stated intervals with final concentrations of 0.25 mg·L^{-1} and 50 mg·L^{-1}, respectively. The open-circuit potentials of the catalysts were monitored by chronopotentiometry. The stable equilibrium potentials after adding PMS were defined as the oxidation potential of the catalyst–PMS* complex. Linear sweep voltammetry curves with/without BPA addition in the electrolyte were compared to determine the oxidation potential of BPA.

Pilot-Scale Experiment for Water Treatment with ZnFeMnO$_4$ Catalyst. Polyester fiber balls (about 3 cm in diameter) were immersed in 0.5 L aqueous solution with 1 g dispersed ZnFeMnO$_4$ powder. This solution was then ultrasonicated for 30 min and dried at 200 °C for 6 h to obtain the catalyst fiber balls. In

order to avoid the escape of the catalyst powder from the fibers during the continuous-flow operation, the fiber balls obtained above were repeatedly immersed in pure water for three times to obtain the final products (with catalyst loading of ~10 mg per fiber ball). Tap water with spiked BPA was used as the simulated wastewater, and a catalytic column reactor was filled with ZnFeMnO$_4$-fiber balls. The blank fiber balls on the top layer were used to reject the catalyst particles that are washed off from the carriers. The oxidation reaction occurs when the BPA- and PMS-containing solution passes through the porous catalyst-loaded fiber balls in the fixed bed at a flow rate of 50 mL·min^{-1} and a hydraulic retention time of ~13.3 min. When the effluent reached 1 L, the concentration of BPA in the effluent was measured to evaluate the treatment performance of the system. The TON and TOF were calculated according to Eqs. **8** and **9**, respectively.

$$TON = N_{BPA}/n_{cat} \qquad [8]$$

$$TOF = TON/t, \qquad [9]$$

where N_{BPA} is the total amount of BPA (moles) removed after treatment of 5 L feed water, n_{cat} is the total amount of ZnFeMnO$_4$ (moles) in the column reactor, and t is the total reaction time.

Theoretical Calculation Studies. Spin-polarized DFT calculations were performed with the Vienna Ab initio Simulation Package (VASP) (Version 5.4.1) (62, 63). The projector augmented-wave pseudopotential was employed to simulate the interactions between ions and valence electrons. Perdew–Burke–Ernzerhof function within the generalized gradient approximation approach (GGA-PBE) was used to describe the exchange and correlation effect (63–65). The GGA + U calculations were performed with U$_{eff}$ (U$_{eff}$ = Coulomb U − exchange J) values of 4.0 and 5.3 eV for Mn and Fe, respectively (66, 67). The plane-wave energy cutoff was set to 500 eV with the Γ-centered Monkhorst–Pack grids (68). The threshold and maximum force on each atom were 10^{-5} eV and 0.03 eV·Å^{-1} for self-consistent calculation, respectively, and further accurate to 10^{-6} eV and 0.01 eV·Å^{-1} to calculate electronic properties. Van der Waals correction was included by using the DFT-D3 method (69).

The distribution of the cations in the bulk model was determined by the Rietveld refinement of the XRD data. After optimization, the seven-layer slabs separated by a 15-Å vacuum space were used to represent the catalyst surface with the coexposed (110) facet of the catalysts measured from the HRTEM. To investigate the PMS activation activity, the PDOS, bader charges, difference charge density, and adsorption energy were analyzed. The Mn e$_g$ and O 2p centers were determined by taking the weighted mean energy of their PDOS and considering the spin selectivity. The bader charges were calculated following a reported method (70). The charge density wave is defined as dρ = ρ(scf) − ρ(atom), where ρ(scf) denotes the charge density after self-consistent field calculation and ρ(atom) denotes the charge density of the frozen atoms. The difference charge density during PMS adsorption is defined as dρ = ρ(system) − ρ(slab) − ρ(PMS), where ρ(system), ρ(slab), and ρ(PMS) denote the charge density of the whole system, the sole slab, and the frozen PMS, respectively. In addition, the adsorption energy of PMS molecule is defined as E$_{ad}$ = E$_{tot}$ − E$_{slab}$ − E$_{PMS}$, where E$_{slab}$, E$_{PMS}$, and E$_{tot}$ correspond to the energies of the bare slab, the isolated PMS molecule, and the slab-PMS system, respectively.

Author affiliations: ^{a}Chinese Academy of Sciences Key Laboratory of Urban Pollutant Conversion, Department of Environmental Science and Engineering, University of Science & Technology of China, Hefei 230026, China; ^{b}University of Science and Technology of China–City University of Hong Kong Joint Advanced Research Center, Suzhou Institute for Advanced Study, Suzhou 215123, China; ^{c}Department of Materials Science and Engineering, City University of Hong Kong, Hong Kong SAR, China; and ^{d}Nano Science and Technology Institute, University of Science & Technology of China, Suzhou 215123, China

1. B. C. Hodges, E. L. Cates, J.-H. Kim, Challenges and prospects of advanced oxidation water treatment processes using catalytic nanomaterials. *Nat. Nanotechnol.* **13**, 642–650 (2018).
2. S. Gligorovski, R. Strekowski, S. Barbati, D. Vione, Environmental implications of hydroxyl radicals (● OH). *Chem. Rev.* **115**, 13051–13092 (2015).
3. J. Lee, U. von Gunten, J.-H. Kim, Persulfate-based advanced oxidation: Critical assessment of opportunities and roadblocks. *Environ. Sci. Technol.* **54**, 3064–3081 (2020).
4. J. Ding et al., Transformation of acetaminophen in solution containing both peroxymonosulfate and chlorine: Performance, mechanism, and disinfection by-product formation. *Water Res.* **189**, 116605 (2021).
5. K. Liu, J. Lu, Y. Ji, Formation of brominated disinfection by-products and bromate in cobalt catalyzed peroxymonosulfate oxidation of phenol. *Water Res.* **84**, 1–7 (2015).
6. D.-N. Pei, C. Liu, A.-Y. Zhang, X.-Q. Pan, H.-Q. Yu, In situ organic Fenton-like catalysis triggered by anodic polymeric intermediates for electrochemical water purification. *Proc. Natl. Acad. Sci. U.S.A.* **117**, 30966–30972 (2020).
7. Z. Yang, J. Qian, A. Yu, B. Pan, Singlet oxygen mediated iron-based Fenton-like catalysis under nanoconfinement. *Proc. Natl. Acad. Sci. U.S.A.* **116**, 6659–6664 (2019).
8. W. Ren et al., Insights into the electron-transfer regime of peroxydisulfate activation on carbon nanotubes: The role of oxygen functional groups. *Environ. Sci. Technol.* **54**, 1267–1275 (2020).
9. J. Miao et al., Spin-state-dependent peroxymonosulfate activation of single-atom M-N moieties via a radical-free pathway. *ACS Catal.* **11**, 9569–9577 (2021).
10. W. Ren et al., The intrinsic nature of persulfate activation and N-doping in carbocatalysis. *Environ. Sci. Technol.* **54**, 6438–6447 (2020).
11. L. Yu et al., Interface stabilization of undercoordinated iron centers on manganese oxides for nature-inspired peroxide activation. *ACS Catal.* **8**, 1090–1096 (2018).
12. W. Wang et al., The confined interlayer growth of ultrathin two-dimensional Fe_3O_4 nanosheets with enriched oxygen vacancies for peroxymonosulfate activation. *ACS Catal.* **11**, 11256–11265 (2021).
13. Z. Wu et al., Core-shell magnetic Fe_3O_4@ Zn/Co-ZIFs to activate peroxymonosulfate for highly efficient degradation of carbamazepine. *Appl. Catal. B* **277**, 119136 (2020).
14. Z. Chen, S. Bi, G. Zhao, Y. Chen, Y. Hu, Enhanced degradation of triclosan by cobalt manganese spinel-type oxide activated peroxymonosulfate oxidation process via sulfate radicals and singlet oxygen: Mechanisms and intermediates identification. *Sci. Total Environ.* **711**, 134715 (2020).
15. C.-X. Li et al., Metal organic framework-derived $CoMn_2O_4$ catalyst for heterogeneous activation of peroxymonosulfate and sulfanilamide degradation. *Chem. Eng. J.* **337**, 101–109 (2018).
16. Y. Ren et al., Sulfate radicals induced from peroxymonosulfate by magnetic ferrospinel MFe_2O_4 (M = Co, Cu, Mn, and Zn) as heterogeneous catalysts in the water. *Appl. Catal. B* **165**, 572–578 (2015).
17. J. Deng et al., Magnetic $MnFe_2O_4$ activated peroxymonosulfate processes for degradation of bisphenol A: Performance, mechanism and application feasibility. *Appl. Surf. Sci.* **459**, 138–147 (2018).
18. J. Du, J. Bao, Y. Liu, S. H. Kim, D. D. Dionysiou, Facile preparation of porous Mn/Fe_3O_4 cubes as peroxymonosulfate activating catalyst for effective bisphenol A degradation. *Chem. Eng. J.* **376**, 119193 (2019).
19. H. Lin et al., Degradation of bisphenol A by activating peroxymonosulfate with $Mn_{0.6}Zn_{0.4}Fe_2O_4$ fabricated from spent Zn-Mn alkaline batteries. *Chem. Eng. J.* **364**, 541–551 (2019).
20. G.-X. Huang, C.-Y. Wang, C.-W. Yang, P.-C. Guo, H.-Q. Yu, Degradation of bisphenol A by peroxymonosulfate catalytically activated with $Mn_{1.8}Fe_{1.2}O_4$ nanospheres: Synergism between Mn and Fe. *Environ. Sci. Technol.* **51**, 12611–12618 (2017).
21. M.-K. Ke et al., Interface-promoted direct oxidation of *p*-arsanilic acid and removal of total arsenic by the coupling of peroxymonosulfate and Mn-Fe-mixed oxide. *Environ. Sci. Technol.* **55**, 7063–7071 (2021).
22. Y. Lu et al., Identifying the geometric site dependence of spinel oxides for the electrooxidation of 5-hydroxymethylfurfural. *Angew. Chem. Int. Ed. Engl.* **59**, 19215–19221 (2020).
23. X. Xie, Y. Li, Z.-Q. Liu, M. Haruta, W. Shen, Low-temperature oxidation of CO catalysed by $Co_{(3)}O_{(4)}$ nanorods. *Nature* **458**, 746–749 (2009).
24. Y. Zhou et al., Superexchange effects on oxygen reduction activity of edge-sharing $[Co_xMn_{1−x}O_6]$ octahedra in spinel oxide. *Adv. Mater.* **30**, 1705407 (2018).
25. Z. Y. Guo et al., Mn-O covalency governs the intrinsic activity of Co-Mn spinel oxides for boosted peroxymonosulfate activation. *Angew. Chem. Int. Ed. Engl.* **60**, 274–280 (2021).
26. N. Zhang et al., Cation-deficient spinel $ZnMn_2O_4$ cathode in Zn ($CF_3SO_3)_2$ electrolyte for rechargeable aqueous Zn-ion battery. *J. Am. Chem. Soc.* **138**, 12894–12901 (2016).
27. J. Goodenough, A. Loeb, Theory of ionic ordering, crystal distortion, and magnetic exchange due to covalent forces in spinels. *Phys. Rev.* **98**, 391 (1955).
28. J. B. Goodenough, A. Wold, R. Arnott, N. Menyuk, Relationship between crystal symmetry and magnetic properties of ionic compounds containing Mn^{3+}. *Phys. Rev.* **124**, 373 (1961).
29. T. Murata, Y. Kozuka, M. Uchida, M. Kawasaki, Magnetic properties of spin frustrated spinel $ZnFe_2O_4/ZnCr_2O_4$ superlattices. *J. Appl. Phys.* **118**, 193901 (2015).
30. Y.-H. Guan et al., Efficient degradation of atrazine by magnetic porous copper ferrite catalyzed peroxymonosulfate oxidation via the formation of hydroxyl and sulfate radicals. *Water Res.* **47**, 5431–5438 (2013).
31. T. Zhang, W. Li, J.-P. Croué, A non-acid-assisted and non-hydroxyl-radical-related catalytic ozonation with ceria supported copper oxide in efficient oxalate degradation in water. *Appl. Catal. B* **121**, 88–94 (2012).
32. L. Zhang et al., Carbon nitride supported high-loading Fe single-atom catalyst for activating of peroxymonosulfate to generate $^1O_2$ with 100% selectivity. *Angew. Chem. Int. Ed.* **60**, 21751–21755 (2021).
33. F. Chen et al., Efficient decontamination of organic pollutants under high salinity conditions by a nonradical peroxymonosulfate activation system. *Water Res.* **191**, 116799 (2021).
34. H. Zhang, C.-H. Huang, Oxidative transformation of triclosan and chlorophene by manganese oxides. *Environ. Sci. Technol.* **37**, 2421–2430 (2003).
35. W. Ren et al., Origins of electron-transfer regime in persulfate-based nonradical oxidation processes. *Environ. Sci. Technol.* **56**, 78–97 (2022).
36. J. Miao, J. Geng, P. J. J. Alvarez, M. Long II, N-doped porous carbon derived from polydopamine-coated graphitic carbon nitride for efficient nonradical activation of peroxymonosulfate. *Environ. Sci. Technol.* **54**, 8473–8481 (2020).
37. S. Zhu et al., Catalytic removal of aqueous contaminants on N-doped graphitic biochars: Inherent roles of adsorption and nonradical mechanisms. *Environ. Sci. Technol.* **52**, 8649–8658 (2018).
38. K. Z. Huang, H. Zhang, Direct electron-transfer-based peroxymonosulfate activation by iron-doped manganese oxide (δ-MnO_2) and the development of galvanic oxidation processes (GOPs). *Environ. Sci. Technol.* **53**, 12610–12620 (2019).
39. W. Ren et al., Activation of peroxydisulfate on carbon nanotubes: Electron-transfer mechanism. *Environ. Sci. Technol.* **53**, 14595–14603 (2019).
40. P. Shao et al., Potential difference driving electron transfer via defective carbon nanotubes toward selective oxidation of organic micropollutants. *Environ. Sci. Technol.* **54**, 8464–8472 (2020).
41. X. Duan, H. Sun, Z. Shao, S. Wang, Nonradical reactions in environmental remediation processes: Uncertainty and challenges. *Appl. Catal. B* **224**, 973–982 (2018).
42. C. Du et al., Monodisperse palladium sulfide as efficient electrocatalyst for oxygen reduction reaction. *ACS Appl. Mater. Interfaces* **10**, 753–761 (2018).
43. B. Zhang et al., High-valence metals improve oxygen evolution reaction performance by modulating 3d metal oxidation cycle energetics. *Nat. Catal.* **3**, 985–992 (2020).
44. M. P. de Jong et al., Evidence for Mn^{2+} ions at surfaces of $La_{0.7}Sr_{0.3}MnO_3$ thin films. *Phys. Rev. B Condens. Matter Mater. Phys.* **71**, 014434 (2005).
45. F. M. F. de Groot et al., Oxygen 1s x-ray-absorption edges of transition-metal oxides. *Phys. Rev. B Condens. Matter* **40**, 5715–5723 (1989).
46. J. Li, D. Chu, H. Dong, D. R. Baker, R. Jiang, Boosted oxygen evolution reactivity by igniting double exchange interaction in spinel oxides. *J. Am. Chem. Soc.* **142**, 50–54 (2020).
47. D. A. Kuznetsov et al., Tuning redox transitions via inductive effect in metal oxides and complexes, and implications in oxygen electrocatalysis. *Joule* **2**, 225–244 (2018).
48. X. Zhang et al., Ultrathin nanosheets of MAX phases with enhanced thermal and mechanical properties in polymeric compositions: $Ti_3Si_{0.75}Al_{0.25}C_2$. *Angew. Chem. Int. Ed.* **125**, 4457–4461 (2013).
49. S. Chen et al., Delocalized spin states in 2D atomic layers realizing enhanced electrocatalytic oxygen evolution. *Adv. Mater.* **29**, 1701687 (2017).
50. K. Xu et al., Metallic nickel nitride nanosheets realizing enhanced electrochemical water oxidation. *J. Am. Chem. Soc.* **137**, 4119–4125 (2015).
51. B. Bachiller-Baeza, J. Anderson, FTIR and reaction studies of styrene and toluene over silica-zirconia-supported heteropoly acid catalysts. *J. Catal.* **212**, 231–239 (2002).
52. Y. Sun, G. Chen, S. Xi, Z. J. Xu, Catalytically influential features in transition metal oxides. *ACS Catal.* **11**, 13947–13954 (2021).
53. X. Zhou et al., Identification of Fenton-like active Cu sites by heteroatom modulation of electronic density. *Proc. Natl. Acad. Sci. U.S.A.* **119**, e2119492119 (2022).
54. L. Gao et al., *Operando* unraveling photothermal-promoted dynamic active-sites generation in $NiFe_2O_4$ for markedly enhanced oxygen evolution. *Proc. Natl. Acad. Sci. U.S.A.* **118**, e2023421118 (2021).
55. Y. Yang et al., Octahedral spinel electrocatalysts for alkaline fuel cells. *Proc. Natl. Acad. Sci. U.S.A.* **116**, 24425–24432 (2019).
56. N. J. O'Connor, A. Jonayat, M. J. Janik, T. P. Senftle, Interaction trends between single metal atoms and oxide supports identified with density functional theory and statistical learning. *Nat. Catal.* **1**, 531–539 (2018).
57. J. Li et al., Understanding of the oxidation behavior of benzyl alcohol by peroxymonosulfate via carbon nanotubes activation. *ACS Catal.* **10**, 3516–3525 (2020).
58. J. Li et al., Cobalt single atoms embedded in nitrogen-doped graphene for selective oxidation of benzyl alcohol by activated peroxymonosulfate. *Small* **17**, e2004579 (2021).
59. S. Y. Park et al., $CaSnO_3$: An electrocatalyst for two-electron water oxidation reaction to form H_2O_2. *ACS Energy Lett.* **4**, 352–357 (2018).
60. B. H. Toby, EXPGUI, a graphical user interface for GSAS. *J. Appl. Cryst.* **34**, 210–213 (2001).
61. A. Jawad et al., Tuning of persulfate activation from a free radical to a nonradical pathway through the incorporation of non-redox magnesium oxide. *Environ. Sci. Technol.* **54**, 2476–2488 (2020).
62. G. Kresse, J. Furthmüller, Efficient iterative schemes for ab initio total-energy calculations using a plane-wave basis set. *Phys. Rev. B Condens. Matter* **54**, 11169–11186 (1996).
63. G. Kresse, D. Joubert, From ultrasoft pseudopotentials to the projector augmented-wave method. *Phys. Rev. B Condens. Matter Mater. Phys.* **59**, 1758 (1999).
64. J. P. Perdew, K. Burke, M. Ernzerhof, Generalized gradient approximation made simple. *Phys. Rev. Lett.* **77**, 3865–3868 (1996).
65. P. E. Blöchl, Projector augmented-wave method. *Phys. Rev. B Condens. Matter* **50**, 17953–17979 (1994).
66. S. Dudarev, G. Botton, S. Savrasov, C. Humphreys, A. Sutton, Electron-energy-loss spectra and the structural stability of nickel oxide: An LSDA+U study. *Phys. Rev. B Condens. Matter Mater. Phys.* **57**, 1505 (1998).
67. H. Li et al., Metal–oxygen hybridization determined activity in spinel-based oxygen evolution catalysts: A case study of $ZnFe_{2−x}Cr_xO_4$. *Chem. Mater.* **30**, 6839–6848 (2018).
68. H. J. Monkhorst, J. D. Pack, Special points for Brillouin-zone integrations. *Phys. Rev. B* **13**, 5188 (1976).
69. S. Grimme, J. Antony, S. Ehrlich, H. Krieg, A consistent and accurate ab initio parametrization of density functional dispersion correction (DFT-D) for the 94 elements H-Pu. *J. Chem. Phys.* **132**, 154104 (2010).
70. E. Sanville, S. D. Kenny, R. Smith, G. Henkelman, Improved grid-based algorithm for Bader charge allocation. *J. Comput. Chem.* **28**, 899–908 (2007).